

# Numerical investigation of flows around an axisymmetric body of revolution by using Reynolds-stress model based hybrid Reynolds-averaged Navier–Stokes/large eddy simulation

Cite as: Phys. Fluids **33**, 085115 (2021); <https://doi.org/10.1063/5.0058016>

Submitted: 26 May 2021 • Accepted: 14 July 2021 • Published Online: 05 August 2021

Yi Liu, Zhiteng Zhou,  Lixing Zhu, et al.



View Online



Export Citation



CrossMark

## ARTICLES YOU MAY BE INTERESTED IN

[Full-scale simulation of self-propulsion for a free-running submarine](#)

Physics of Fluids **33**, 047103 (2021); <https://doi.org/10.1063/5.0041334>

[Influence of jet flow on the hydrodynamic and noise performance of propeller](#)

Physics of Fluids **33**, 065123 (2021); <https://doi.org/10.1063/5.0051326>

[Reynolds number effect on statistics of turbulent flows over periodic hills](#)

Physics of Fluids **33**, 105124 (2021); <https://doi.org/10.1063/5.0062786>

**APL Machine Learning**

Open, quality research for the networking communities

**Now Open for Submissions**

LEARN MORE



# Numerical investigation of flows around an axisymmetric body of revolution by using Reynolds-stress model based hybrid Reynolds-averaged Navier–Stokes/large eddy simulation

Cite as: Phys. Fluids **33**, 085115 (2021); doi: [10.1063/5.0058016](https://doi.org/10.1063/5.0058016)

Submitted: 26 May 2021 · Accepted: 14 July 2021 ·

Published Online: 5 August 2021



View Online



Export Citation



CrossMark

Yi Liu,<sup>1,2</sup> Zhiteng Zhou,<sup>1,2</sup> Lixing Zhu,<sup>1,2</sup>  and Shizhao Wang<sup>1,2,a)</sup> 

## AFFILIATIONS

<sup>1</sup>LNM, Institute of Mechanics, Chinese Academy of Sciences, Beijing 100190, China

<sup>2</sup>School of Engineering Sciences, University of Chinese Academy of Sciences, Beijing 10049, China

<sup>a)</sup> Author to whom correspondence should be addressed: [wangsz@lnm.imech.ac.cn](mailto:wangsz@lnm.imech.ac.cn)

## ABSTRACT

Flows around an axisymmetric body of revolution at a zero yaw angle were studied using a hybrid Reynolds-averaged Navier–Stokes (RANS)/large eddy simulation (LES) approach, which employed a full Reynolds stress model (RSM) in the RANS branch with the aim of accounting for the Reynolds stress anisotropy, streamline curvature, and flow separations in the boundary layer. The SUBOFF model without appendages was applied to conduct the simulations, and the Reynolds number based on the free-stream velocity and the length of the body is  $Re_L = 1.2 \times 10^6$ . The results, including time-averaged  $C_p$ ,  $C_f$ , and velocity statistics, were compared with the experimental data and wall-resolved LES results available in the literature, and the overall agreement of the comparisons was satisfactory. To assess the performance of the RSM-based hybrid RANS/LES approach, we carried out shear-stress transport-based hybrid RANS/LES approach simulations under identical free-stream conditions for comparison. The sensitivity of the hybrid RANS/LES approach to the RANS models was observed for separated flow with surface curvature and adverse pressure gradient-induced separation. The RSM-based hybrid RANS/LES approach was found to provide a better prediction for the unsteady flows near the stern. That is because the effects of the streamline curvature and the strong interactions between individual stresses can be captured by the exact production terms in the RSM-based hybrid RANS/LES approach. These effects are important for predicting the development of turbulent boundary layers along the stern.

Published under an exclusive license by AIP Publishing. <https://doi.org/10.1063/5.0058016>

## I. INTRODUCTION

Flows around the sterns of ships and other underwater vehicles are often very complicated, with vortices interacting with the boundary layer and unsteady separations. This scenario is particularly true for the boundary flows affected by pressure gradients and the hull curvature, which may subsequently lead to flow separations resulting in a significant source of noise and a serious distortion of the propeller inflow.<sup>1–5</sup>

Numerous experimental and numerical studies have investigated turbulent flows near sterns.<sup>6–13</sup> In particular, Huang *et al.*<sup>14</sup> conducted an experiment focusing on the complex flow over the stern and provided detailed measurements in several configurations, including SUBOFF body with and without appendages (hereafter referred to as

SUBOFF). Their results showed that the boundary layer on the stern is strongly affected by the adverse pressure gradient. More recent experiments on an axisymmetric body based on the SUBOFF model were conducted by Jiménez *et al.*<sup>15,16</sup> to investigate the turbulence in the wake, where a bimodal distribution of the turbulent stress was found. Posa and Balaras<sup>17</sup> presented a wall-resolved large eddy simulation (LES) of the SUBOFF body with appendages, and their results confirmed the complexity of the stern flow and traced the source of the bimodal behavior of the turbulent stresses in the wake back to the thick boundary layer over the stern. Recently, Kumar and Mahesh<sup>18</sup> conducted an analysis of near-wall flow structures and the wake evolution on the bare hull SUBOFF body using wall-resolved LES, in which good agreement with the experiments was obtained. To reveal the

effects of Reynolds numbers on the structure of the boundary layer over the stern, Posa and Balaras<sup>19</sup> extended the LES of flows around SUBOFF with appendages to  $Re_L = 1.2 \times 10^7$ , in which  $8.1 \times 10^9$  nodes were employed to resolve the turbulent flows near the stern. Their study showed the turbulent boundary layer over the stern was severely affected by the adverse pressure gradient almost independent of the Reynolds number. Zhou *et al.*<sup>20</sup> performed an LES of an axisymmetric body of revolution, and the space-time characteristics of velocity fluctuations in the tail-cone boundary layer were investigated in detail. The predicted velocity statistics were in good agreement with the experimental results and indicated that the development of the tail-cone turbulent boundary layer was insensitive to the near-wall structures upstream. Subsequently, emphasis was placed on the evolution of the turbulent boundary layer over the stern. However, wall-resolved LES is expensive because of the turbulent boundary layer at high Reynolds numbers.<sup>21,22</sup> Especially for ship hydrodynamics, massive computing costs are required because they involve high Reynolds numbers on the order of  $10^6$  at the model scale and  $10^9$  at the full scale, and the flow is characterized by a wide spectrum of turbulent scales.<sup>23–26</sup>

The hybrid Reynolds-averaged Navier–Stokes/large eddy simulation (RANS/LES) approach is an alternative method with high efficiency and acceptable accuracy for turbulent flows at high Reynolds numbers.<sup>27–35</sup> Mokhtarpoor *et al.*<sup>29</sup> made detailed studies on the flows over periodic hill using hybrid RANS/LES method, and their studies proved the advantages of the hybrid method for high Reynolds number flow simulations. Detached eddy simulation (DES) proposed by Spalart *et al.*<sup>31</sup> is a hybrid RANS/LES approach that treats the boundary layers using a RANS (Reynolds-averaged Navier–Stokes) model and applies LES to separated regions. This approach reduces computing costs in comparison with the wall-resolved LES while retaining much of the unsteady feature of the flows. Some shortcomings were reported in hybrid RANS/LES approach, such as erroneous activities of the near-wall damping terms in the LES branch, incursion of the LES branch inside the boundary layer, gray area, and log-layer mismatch. However, these shortcomings have been addressed or alleviated in later revisions, such as delayed DES (DDES),<sup>32</sup> improved DDES (IDDES),<sup>33</sup> and extended DDES.<sup>34</sup> Similar to the work of Spalart, Strelets<sup>35</sup> proposed another DES approach, which is based on the two-equation shear-stress transport (SST) model. Lately, Yin *et al.*<sup>36,37</sup> proposed an adaptive DES approach to study the jet in crossflow, the key structures of the flows are well reproduced comparing with direct numerical simulation data. He *et al.*<sup>38,39</sup> developed a dynamic DDES model based on the  $k - \omega$  SST model, in which the log-layer mismatch problem is alleviated by dynamically computing the model coefficients. The capability of the DES approach has been demonstrated in many test cases. Mylonas and Sayer<sup>40</sup> studied the forces acting on an International America's Cup Class yacht keel model by using LES and DES. Accurate predictions of the forces were obtained for both methods, and characteristics of the flow, such as separation, vortices, and wakes, were well predicted and resolved. Sun *et al.*<sup>41</sup> conducted a DES study on the wake vortex evolution characteristics of full- and model-scale propellers. Usta and Korkut<sup>42</sup> studied unsteady cavitating flows around the hydrofoil and propeller by using DES. In addition to the application in navigation, Wang *et al.*<sup>43</sup> employed the IDDES to study the pulsed blowing on a pitching airfoil for flow controls; Liu and Xiao<sup>44</sup> used the DDES method to investigate the unsteady flows past a

NACA0015 airfoil near stall at high Reynolds numbers; Liu *et al.*<sup>45</sup> performed a series of DDES simulations around a hammerhead payload fairing in the transonic regime; Yao and Davidson<sup>46</sup> conducted both compressible and incompressible IDDES simulations to investigate the cabin window vibration excited by the turbulent wake; the accuracy and efficiency of DES approaches are investigated and demonstrated by these studies. Recently, Xiao and Zhang<sup>47</sup> proposed a modification to SST-based IDDES method and evaluated its performance by a free shear flow. This type of DES approach and its variants, including DDES, adaptive DES, and IDDES, are potentially capable of producing separated flows and the evolution of wakes.<sup>48–50</sup>

Alin *et al.*<sup>51</sup> made a comprehensive investigation on the current capabilities of DES and LES for the underwater vehicles, in which the  $k - \omega$ -based DES appears to somewhat overpredict the magnitude of the velocity fluctuations. We presume that such over-predictions might be due to the utilized RANS model involving the eddy-viscosity assumption. A thorough study of DES methods presented by Mockett<sup>30</sup> showed that the sensitivity of DES to the RANS model cannot be negligible for flow separation from smooth surfaces, and the model sensitivity would be high for flows with sensitive turbulent separation from curved surfaces. This finding elucidated the importance of RANS modeling in DESs. However, most of the previous approaches are based on a one-equation model or two-equation model, which invokes the eddy-viscosity assumption for modeling Reynolds stress. Especially for applications in system rotation and curved bounded layers, these models are usually utilized but still require a correction to yield the proper shear stress. Relatively thick and curved boundary layers could make using complex models necessary.<sup>27</sup> Abandoning the isotropic eddy-viscosity hypothesis, the Reynolds stress model (RSM) closes the RANS equations by solving the transport equations for Reynolds stresses. Since the RSM accounts for a more detailed representation of the flow physics, such as the effects of streamline curvature, swirling, rotation, and rapid changes in strain rate, this approach has greater potential to give accurate predictions for complex flows.<sup>52–54</sup> Thus, the application of RSM in hybrid RANS/LES approaches might be helpful to improve the performance of hybrid approaches for predicting the complex flows that are dominated by the surface curvature.

The objects of this work are to investigate the RSM model in the hybrid RANS/LES approach for high Reynolds numbers flows around SUBOFF and analyze the capability of RSM-based hybrid approach in predicting the effects of surface curvature on the turbulent boundary layers. The reminder of this paper is organized as follows: The RSM-based hybrid RANS/LES approach and basic numerical methods were briefly described in Sec. II. This was followed by the computational results and detailed analysis of the instantaneous and statistical data (in Sec. III). Especially, the models' capability in predicting the effects of surface curvature was investigated in Sec. III D. Finally, the summary and conclusions were presented in Sec. IV.

## II. NUMERICAL METHOD

### A. Governing equations

The filtered Navier–Stokes equations for compressible flows are given below,<sup>55</sup>

$$\frac{\partial \bar{\rho}}{\partial t} + \frac{\partial}{\partial x_k} (\bar{\rho} \tilde{u}_k) = 0, \quad (1a)$$

$$\frac{\partial(\bar{\rho}\tilde{u}_i)}{\partial t} + \frac{\partial}{\partial x_k}(\bar{\rho}\tilde{u}_i\tilde{u}_k) + \frac{\partial}{\partial x_k}(\bar{\rho}\tilde{R}_{ik}) = -\frac{\partial\bar{p}}{\partial x_i} + \frac{\partial\bar{\tau}_{ik}}{\partial x_k}, \quad (1b)$$

$$\begin{aligned} \frac{\partial(\bar{\rho}\tilde{E})}{\partial t} + \frac{\partial}{\partial x_k}(\bar{\rho}\tilde{H}\tilde{u}_k) + \frac{\partial}{\partial x_k}(\bar{\rho}\tilde{R}_{ik}\tilde{u}_i) \\ = \frac{\partial(\bar{\tau}_{ik}\tilde{u}_i)}{\partial x_k} + \bar{\rho}D^{(k)} - \frac{\partial\tilde{q}_k^{(t)}}{\partial x_k}, \end{aligned} \quad (1c)$$

where  $\bar{\varphi}$  denotes simple average and  $\tilde{\varphi} = \overline{\rho\varphi}/\bar{\rho}$  represents the Favre filtered variables.  $\bar{\rho}$ ,  $\bar{p}$ , and  $\tilde{u}_i$  represent the density, pressure, and velocity, respectively. The averaged total energy and total enthalpy are given by  $\tilde{E} = \tilde{e} + 0.5\tilde{u}_i\tilde{u}_i$  and  $\tilde{H} = \tilde{E} + \bar{p}/\bar{\rho}$ .  $n_i$  is the Cartesian component of the exterior surface unit normal vector on the boundary. By convention, the notation  $\bar{\tau}_{ij}$  represents averaged viscous stress, it is described by

$$\bar{\tau}_{ij} = \bar{\mu} \left( \frac{\partial\tilde{u}_i}{\partial x_j} + \frac{\partial\tilde{u}_j}{\partial x_i} - \frac{2}{3}\frac{\partial\tilde{u}_k}{\partial x_k}\delta_{ij} \right). \quad (2)$$

$\bar{\mu}$  is the dynamic viscosity. The heat flux reads

$$\tilde{q}_i = -\lambda\frac{\partial\tilde{T}}{\partial x_i}. \quad (3)$$

$\lambda$  represents the thermal conductivity coefficient. The Reynolds stress tensor is indicated by  $\bar{\rho}\tilde{R}_{ij}$ . The corresponding components of the turbulent heat flux vector are indicated by  $\tilde{q}_i^{(t)} = -\lambda_t\partial\tilde{T}/\partial x_i$ , where  $\lambda_t$  denotes the turbulent thermal conductivity coefficient. The diffusion of specific kinetic turbulence energy is indicated by  $D^{(k)}$ , which is related to the diffusion term of Eq. (4) and given by  $D^{(k)} = 0.5D_{kk}$ . Further details about these terms can be found in the work of Cécora *et al.*<sup>56</sup>

The governing equations are discretized with the cell-centered finite volume method (FVM) on unstructured hybrid meshes composed of hexahedrons, prisms, tetrahedrons, and pyramids (further details are given by Wang and Ye<sup>57</sup>). An in-house computational fluid dynamics solver<sup>45,57–59</sup> is used to solve Eq. (1). The convective flux terms were computed with second-order Roe discretization schemes, and the viscous flux terms were obtained by the reconstructed central scheme. For the Roe scheme, the second-order accuracy was achieved by reconstructing the solution following Frink’s interpolation method.<sup>60</sup> The lower–upper symmetric Gauss–Seidel (LU-SGS) relaxation-based implicit backward-Euler scheme is implemented for steady flow simulation, and a corresponding second-order full implicit dual time scheme is adopted for unsteady flow. An adaptive local time-stepping method was developed to eliminate the adverse influence of some poor-quality grids on solution stability and convergence. In addition, a form of locally adaptive flux blending<sup>61,62</sup> has been implemented in the Roe scheme, ensuring a dominance of low dissipation in the LES region and more stability in the RANS region. For the purpose of large-scale computation, this solver has been parallelized by using a domain decomposition strategy with the MPI (message passing interface) protocol. Nonblocking communications are used to overlap computation with communication and exploit possible performance gains. The details of the numerical methods employed in this work are summarized in Table I.

### B. Hybrid RANS/LES method

A RSM is applied in the RANS branch with the aim of accounting for the Reynolds stress anisotropy, streamline curvature, and swirl

TABLE I. The details of numerical methods.

Governing equations	Three-dimensional, compressible Navier–Stokes equation
Spatial discretization	Cell-centered FVM
Temporal evolution	Lower–upper symmetric Gauss–Seidel (LU-SGS)
Time marching	2nd order, fully implicit dual time scheme
Reconstruction	2nd Roe scheme for inviscid term 2nd central scheme for viscous term
Turbulence model	RSM-based IDDES and SST-based IDDES

emerging in the turbulent boundary layer. The IDDES formulation is based on a modification to the Speziale–Sarkar–Gatski (SSG)/Launder–Reece–Rodi (LRR)- $\omega$  RSM such that the model reduces to its RANS branch near the solid wall and to a subgrid model away from the wall. The SSG/LRR- $\omega$  RSM model,<sup>56</sup> developed by the DLR (Cécora, 2015), is a combination of the Speziale–Sarkar–Gatski model and the Launder–Reece–Rodi model, and the details are shown as follows.

### 1. SSG/LRR- $\omega$ Reynolds stress model in hybrid context

The SSG/LRR- $\omega$  RSM model solves directly for the Reynolds stresses  $\bar{\rho}\tilde{R}_{ij} = \rho u'_i u'_j$ . Here, the superscript  $u'_i$  represents the turbulent velocity fluctuations. The Reynolds stress transport equations are given by

$$\frac{\partial}{\partial t}(\bar{\rho}\tilde{R}_{ij}) + \frac{\partial}{\partial x_k}(\bar{\rho}\tilde{u}_k\tilde{R}_{ij}) = \bar{\rho}P_{ij} + \bar{\rho}\Pi_{ij} - \bar{\rho}\varepsilon_{ij} + \bar{\rho}D_{ij}, \quad (4)$$

where the production tensor  $\bar{\rho}P_{ij}$  is a closed term, because it involves the dependent variable  $\tilde{R}_{ij}$  and given the flow gradients. This term is given by

$$\bar{\rho}P_{ij} = -\bar{\rho}\tilde{R}_{ik}\frac{\partial\tilde{u}_j}{\partial x_k} - \bar{\rho}\tilde{R}_{jk}\frac{\partial\tilde{u}_i}{\partial x_k}. \quad (5)$$

All other terms on the right-hand side of Eq. (4) require modeling. The pressure-strain correlation term is treated by a model developed by Speziale *et al.*<sup>63</sup> This model reads

$$\begin{aligned} \bar{\rho}\Pi_{ij} = & -\left(C_1\bar{\rho}\varepsilon + \frac{1}{2}C_1^*\bar{\rho}P_{kk}\right)\tilde{b}_{ij} + C_2\bar{\rho}\varepsilon\left(\tilde{b}_{ik}\tilde{b}_{kj} - \frac{1}{3}\tilde{b}_{kl}\tilde{b}_{kl}\delta_{ij}\right) \\ & + \left(C_3 - C_3^*\sqrt{\tilde{b}_{kl}\tilde{b}_{kl}}\right)\bar{\rho}\tilde{k}\tilde{S}_{ij}^* \\ & + C_4\bar{\rho}\tilde{k}\left(\tilde{b}_{ik}\tilde{S}_{jk} + \tilde{b}_{jk}\tilde{S}_{ik} - \frac{2}{3}\tilde{b}_{kl}\tilde{S}_{kl}\delta_{ij}\right) \\ & + C_5\bar{\rho}\tilde{k}\left(\tilde{b}_{ik}\tilde{W}_{jk} + \tilde{b}_{jk}\tilde{W}_{ik}\right). \end{aligned} \quad (6)$$

In this equation,  $\tilde{S}_{ij} = \frac{1}{2}\left(\frac{\partial\tilde{u}_i}{\partial x_j} + \frac{\partial\tilde{u}_j}{\partial x_i}\right)$  and  $\tilde{W}_{ij} = \frac{1}{2}\left(\frac{\partial\tilde{u}_i}{\partial x_j} - \frac{\partial\tilde{u}_j}{\partial x_i}\right)$  are the rate-of-strain tensor and the rate-of-rotation tensor, respectively.  $\tilde{S}_{ij}^* = \tilde{S}_{ij} - \frac{1}{3}\frac{\partial\tilde{u}_k}{\partial x_k}\delta_{ij}$  is the mean traceless strain tensor,  $\tilde{b}_{ij} = \frac{\tilde{R}_{ij}}{\tilde{k}} - \frac{2}{3}\delta_{ij}$  is the anisotropy tensor,  $\tilde{k}$  represents turbulence energy that is related

TABLE II. Values of closure coefficients for the pressure-strain correlation term and the diffusion term.

	$\hat{C}_1$	$\hat{C}_1^*$	$\hat{C}_2$	$\hat{C}_3$	$\hat{C}_3^*$	$\hat{C}_4$	$\hat{C}_5$	$\hat{D}$
SSG	1.7	0.9	1.05	0.8	0.65	0.625	0.2	0.22
LRR	1.8	0.0	0.0	0.8	0.0	$[(9C_2^{(LRR)} + 6)/11]^a$	$[(-7C_2^{(LRR)} + 10)/11]^a$	$0.75C_\mu$

<sup>a</sup> $C_2^{(LRR)} = 0.52$ .

to the Reynolds stresses by  $\tilde{k} = 0.5\tilde{R}_{ii}$ , the isotropic dissipation rate  $\varepsilon$  is provided by  $\varepsilon = C_\mu\tilde{k}\omega$  with  $C_\mu = 0.09$ .  $C_1$  to  $C_5$  are model coefficients.

A generalized gradient diffusion model<sup>64</sup> was implemented to compute the diffusion term  $\bar{\rho}D_{ij}$ , which reads

$$\bar{\rho}D_{ij} = \frac{\partial}{\partial x_k} \left[ \left( \bar{\mu}_L \delta_{kl} + D \frac{\bar{\rho}\tilde{k}\tilde{R}_{kl}}{\varepsilon} \right) \frac{\partial \tilde{R}_{ij}}{\partial x_l} \right], \quad (7)$$

where  $D$  is a diffusion coefficient and  $\bar{\mu}_L$  denotes the molecular viscosity that could be provided by the Sutherland law. More details about these terms can be found in Ref. 56. The coefficients  $D$  and  $C_i, C_i^*$  are obtained from Eq. (8), where all coefficients are blended between the SSG and LRR values (listed in Table II) according to the Menter's  $F_1$ -function,

$$\begin{cases} C_i = F_1 \hat{C}_i^{LRR} + (1 - F_1) \hat{C}_i^{SSG}, \\ C_i^* = (1 - F_1) \hat{C}_i^{*,SSG}, \\ D = F_1 \hat{D}^{LRR} + (1 - F_1) \hat{D}^{SSG}. \end{cases} \quad (8)$$

The blending function  $F_1$  is defined by

$$\begin{cases} F_1 = \tanh(\Gamma^4), \\ \Gamma = \min \left[ \max \left( \frac{500\bar{\mu}_L}{\bar{\rho}\omega d^2}, \frac{\sqrt{\tilde{k}}}{C_\mu \omega d} \right), \frac{4\sigma_\omega^{(e)} k \omega}{\sigma_d^{(e)} \max \left( \frac{\partial \tilde{k}}{\partial x_k} \frac{\partial \omega}{\partial x_k}, 1 \times 10^{-20} \right)} \right]. \end{cases} \quad (9)$$

The dissipation  $\bar{\rho}\varepsilon_{ij}$  is modeled by an isotropic tensor as follows:

$$\bar{\rho}\varepsilon_{ij} = \frac{2}{3} \bar{\rho} \delta_{ij} \varepsilon. \quad (10)$$

A hybrid approach involving an interface treatment without synthetic or reconstruction turbulence is employed to switch RANS to LES. This approach uses a dynamic interface criterion based on a local variable. Therefore, the turbulent kinetic energy  $k$  is considered, the isotropic dissipation rate is modified as a length-scale dependent term  $\varepsilon = \tilde{k}^{1.5}/l_{IDDES}$ , and the IDDES length scale  $l_{IDDES}$  is introduced as the switching condition. This length scale is given by

$$l_{IDDES} = \bar{f}_d(1 + f_e)l_{RANS} + (1 - \bar{f}_d)l_{LES}, \quad (11)$$

where  $l_{RANS} = \tilde{k}^{1/2}/C_\mu\omega$  and  $l_{LES} = C_{DES}\Delta$  are the RANS and LES length scales, respectively.  $C_\mu = 0.09$  and  $C_{DES}$  are blended according to  $C_{DES} = F_1 C_{DES,LRR} + (1 - F_1) C_{DES,SSG}$ . The calibration of  $C_{DES,LRR}$  and  $C_{DES,SSG}$  are presented in the Appendix.  $\Delta$  represents the subgrid

length scale, which is defined as  $\Delta = \min[\max(C_w d, C_w \Delta_{max}, d_{wm}), \Delta_{max}]$ ,  $C_w = 0.15$ . Here,  $d$  is the distance to the wall,  $d_{wm}$  is the grid step in the wall-normal direction, and  $\Delta_{max}$  denotes the maximum local grid spacing.  $\bar{f}_d, f_e$  are blending functions, and further details regarding these functions can be found in Ref. 65.

### 2. Length-scale equation

To solve the Reynolds stress transport equations, an additional transport equation is required to provide a measure of the dissipation length-scale  $\omega$ . The SSG/LRR- $\omega$  model follows Menter's approach, the so-called baseline (BSL)  $\omega$ -equation, which reads

$$\begin{aligned} \frac{\partial}{\partial t} (\bar{\rho}\omega) + \frac{\partial}{\partial x_k} (\bar{\rho}\tilde{u}_k\omega) = & \alpha_\omega \frac{\omega\bar{\rho}P_{kk}}{2\tilde{k}} - \beta_\omega \bar{\rho}\omega^2 \\ & + \frac{\partial}{\partial x_k} \left[ \left( \bar{\mu}_L + \sigma_\omega \frac{\bar{\rho}\tilde{k}}{\omega} \right) \frac{\partial \omega}{\partial x_k} \right] \\ & + \sigma_d \frac{\bar{\rho}}{\omega} \max \left( \frac{\partial \tilde{k}}{\partial x_k} \frac{\partial \omega}{\partial x_k}, 0 \right). \end{aligned} \quad (12)$$

In Eq. (12), all coefficients [ $\phi = (\alpha_\omega, \beta_\omega, \sigma_\omega, \sigma_d)$ ] are blended between two bounding values (listed in Table III) according to  $\phi = F_1\phi^{(\omega)} + (1 - F_1)\phi^{(e)}$ .

### III. RESULTS AND DISCUSSION

The basic geometry used in the present work was the SUBOFF without appendages (AFF1), which was outlined by Groves *et al.*<sup>66</sup> A layout is presented in Fig. 1, which shows an axisymmetric hull that is composed of a forebody, a parallel middle body, and an afterbody stern. The overall length is  $L = 14.291\ 667$  ft, and the maximum diameter is  $D = 1.666\ 666\ 7$  ft. The freestream conditions are selected according to the work of Posa<sup>17</sup> and Shi,<sup>67</sup> the angle of attack set as  $0^\circ$  and Reynolds number is equal to  $Re_L = 1.2 \times 10^6$  based on the length  $L$ .

#### A. Numerical setup

Figure 2 shows a schematic of the computational domain. The nonreflecting boundary is a hemisphere with a radius of  $100D$  in the front and extends downstream by  $150D$  from the trailing edge.

TABLE III. Bounding values of  $\omega$ -equation coefficients.

	$\alpha_\omega$	$\beta_\omega$	$\sigma_\omega$	$\sigma_d$
$\phi^{(e)}$	0.44	0.0828	0.856	1.712
$\phi^{(\omega)}$	0.5556	0.075	0.5	0.0

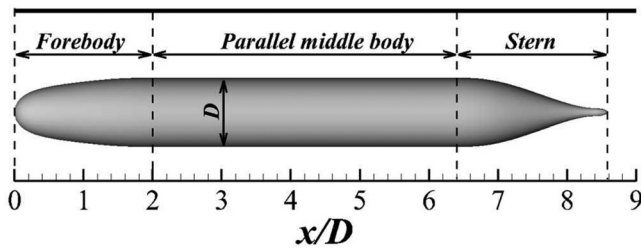


FIG. 1. Schematic of SUBOFF model without appendages.

An adiabatic no-slip wall condition is employed on the hull surface. To determine the mesh convergence, three typical unstructured grids with different resolutions were generated for comparison. The first layer spacing of all grids was chosen using the approach of Cummings *et al.*,<sup>68</sup> such that the average  $y^+ \leq 0.8$  and the growth rate in the boundary layer is 1.18. The primary grid, which will be referred to as the medium-density grid (MDG), consisted of  $37 \times 10^6$  cells. Figure 2(b) shows the topology of the mesh near the stern. The grid is locally refined in the boundary layer and the wake areas, in particular, close to the afterbody cap to properly model the shear layer instability, since the wake of the hull is sensitive to the properties of the stern boundary layer. As shown in Fig. 2(b), an O-H topology was set up in the wake region;  $N_\phi = 380$  points are used in the azimuthal direction, and  $N_x = 630$  points are employed in the streamwise direction to discretize the mixing layer developing from the stern. The two additional grids were generated with the same topology, but the cell spacing was altered such that the total cell counts were approximately  $23 \times 10^6$  cells [referred to as the low-density grid (LDG)] and  $56 \times 10^6$  cells [referred to as the high-density grid (HDG)]. The main features of grids in terms of the number of points and grid parameters are summarized in Table IV.

All the generated grids were employed to perform the simulations with the same free-stream conditions. A nondimensional time step  $\Delta t^* = 0.0007$  ( $\Delta t^* = \Delta t \cdot u_0/L$ , where,  $u_0$  denotes the free-stream velocity and  $\Delta t$  is the dimensional time step size) was used. Data were gathered over three flow-through times after the initial

TABLE IV. Details of the grids properties.

Grids	LDG	MDG	HDG
Total number of cells	$2.3 \times 10^7$	$3.7 \times 10^7$	$5.6 \times 10^7$
$N_\phi$ (in the azimuthal direction)	290	380	450
$N_x$ (in the streamwise direction)	500	630	760

transient stage. The effects of the grid resolution on the time-averaged pressure coefficient [(a)  $C_p$ ] and skin-friction coefficient [(b)  $C_f$ ] distributions were plotted in Fig. 3, which shows that  $C_p$  converges more quickly than  $C_f$  as the grid refinement and  $C_p$  distributions are almost identical for all grids. The definition of the flow quantities investigated in this work is listed in Table V, where the time-averaged pressure ( $C_p$ ) and skin-friction ( $C_f$ ) coefficients are computed as follows:

$$C_p = \frac{p - p_\infty}{0.5\rho_\infty u_0^2}, \quad \text{and} \quad C_f = \frac{\tau_w}{0.5\rho_\infty u_0^2}. \quad (13)$$

$p_\infty$  is the free-stream pressure,  $\rho_\infty$  represents the density of fluid at the far field.  $\tau_w$  and  $p$  represent the time-averaged wall shear stress and pressure, respectively. Figure 3(b) shows the distribution of  $C_f$ , and the differences are negligible moving from MDG to HDG, which confirms that the grid converges at MDG. Thus, the MDG grid was used as a baseline mesh for all further computations.

**B. Overview of the flow**

The instantaneous flow structures are visualized by the isosurface of the  $Q$ -criterion<sup>69</sup> in Fig. 4.  $Q$  is the second invariant velocity gradient tensor defined as  $Q = 0.5(\Omega_{ij}\Omega_{ij} - S_{ij}S_{ij})$ , where  $\Omega_{ij}$  and  $S_{ij}$  denote the antisymmetric and symmetric components of  $\nabla u$ , respectively. As shown in Fig. 4, close to the stern, one can identify a sequence of vortical structures that interact with each other as they are convected downstream and become complex 3D vortices in the wake. A global view of the axial velocity, pressure coefficient, and vorticity magnitude field in the XZ plane is shown in Fig. 5, where the contour of axial velocity [Fig. 5(a)] shows that the axisymmetric turbulent boundary layer gradually thickens due to the reverse pressure gradient on the stern. The axial velocity undergoes a significant deceleration and

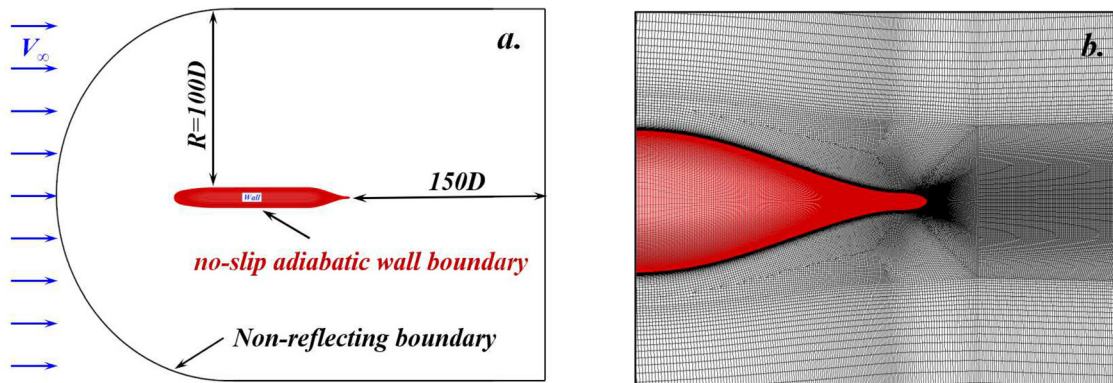


FIG. 2. Computational grid used for the SUBOFF AFF1 hull. (a) The computational domain and the employed boundary conditions. (b) Topology of the grid in the vicinity of aft; the grid is locally refined in the wake region.

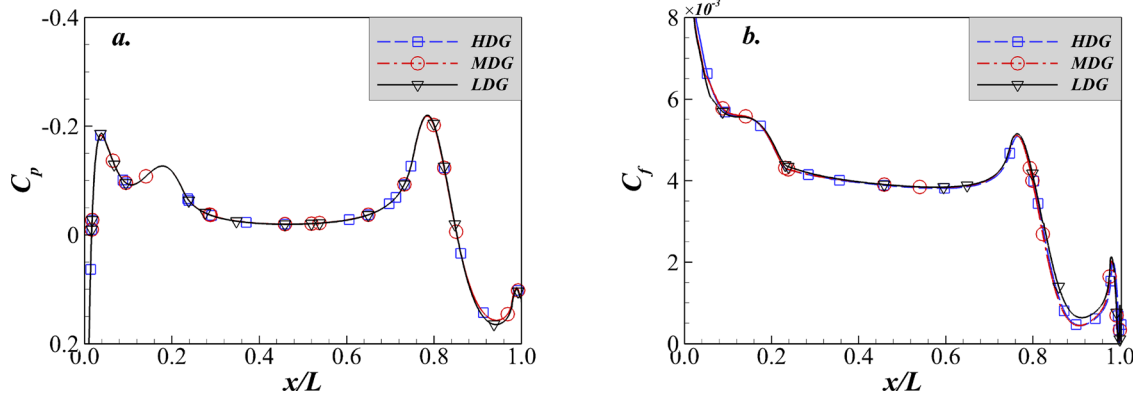


FIG. 3. Time-averaged pressure coefficient  $C_p$  (a) and skin-friction coefficient  $C_f$  (b) distributions for various density grids.

eventually separates to form the wake. In the wake region, the pressure gradient is negligible away from the stern, while the pressure fluctuations induced by vortical structures from upstream can be observed. The contour of vorticity magnitude in Fig. 5(c) shows the regions of intense turbulent activity, which are mainly the hull boundary layer and the wake. The magnitude of the vorticity decreases due to the turbulence dissipation as it moves downstream in the wake.

C. Distribution of forces and velocity

The predicted hull pressure and skin-friction coefficients were plotted against measured data and available LES results in Fig. 6. The experimental data presented by Huang *et al.*<sup>14</sup> and computations presented by Posa and Balaras<sup>17</sup> are included. Computation results come from a wall-resolved LES simulation of the flow around the SUBOFF with appendage model at a Reynolds number of  $Re_L = 1.2 \times 10^6$ . To assess the performance of the RSM-based IDDES, an SST-based IDDES simulation under identical free-stream conditions is conducted, and the results referred to as SST-based IDDES are also plotted in the comparisons. The predicted  $C_p$  profiles [in Fig. 6(a)] do not show differences between SST-based IDDES and RSM-based IDDES. Both are in good agreement with both the measurements by Huang *et al.*<sup>14</sup> and the wall-resolved LES results of Posa,<sup>17</sup> including the levels of  $C_p$  at the bow and at the middle section, as well as the details of  $C_p$  at the tapered stern region. Figure 6(b) represents the comparison

between the experimental data and computed  $C_f$  along the meridian line of the hull. According to the work of Posa and Balaras<sup>17</sup> and Kumar and Mahesh,<sup>18</sup> the skin-friction coefficient  $C_f$  of the experiments is scaled to the  $Re$  of the simulation using a scaling law ( $C_f \sim Re^{-0.2}$ ) based on the measurements of Huang *et al.*<sup>14</sup> Huang *et al.* also reported a measurement uncertainty of  $\pm 0.0002$  for  $C_f$ , which is indicated by error bars in Fig. 6(b). Qualitatively, the evolution of  $C_f$  at the middle section and at the stern are well reproduced by simulations. A gradual increase in  $C_f$  is observed toward the stern due to the flow acceleration caused by the convex surface of the hull.  $C_f$  decreases at the stern due to the presence of flow separation, as shown in Fig. 5. Overall, the results of both SST-based IDDES and RSM-based IDDES show good agreement with the experiments.

The time-averaged axial and radial velocity profiles at four streamwise locations,  $x/L = 0.904, 0.927, 0.956,$  and  $0.978$ , on the stern are compared with the experimental data of Huang *et al.*<sup>14</sup> and LES results presented by Kumar and Mahesh<sup>18</sup> in Figs. 7(a) and 7(b), respectively. Computation results come from a wall-resolved LES of the flow around the bare hull SUBOFF at a Reynolds number equal to  $Re_L = 1.1 \times 10^6$ . The development of the boundary layer over the stern is properly captured, flow separation results in thickening of the hull boundary layer on the stern, and evidence can be found in those

TABLE V. The flow quantities investigated in this work.

Symbol	Explanation
$C_p$	Time-averaged pressure coefficient
$C_f$	Time-averaged skin-friction coefficient
$U$	Streamwise velocity
$u$	Time-averaged velocity in axial direction
$u_r$	Time-averaged velocity in radial direction
$u_{rms}$	RMS-velocity in axial direction
$u_{r,rms}$	RMS-velocity in radial direction
TKE	Turbulent kinetic energy

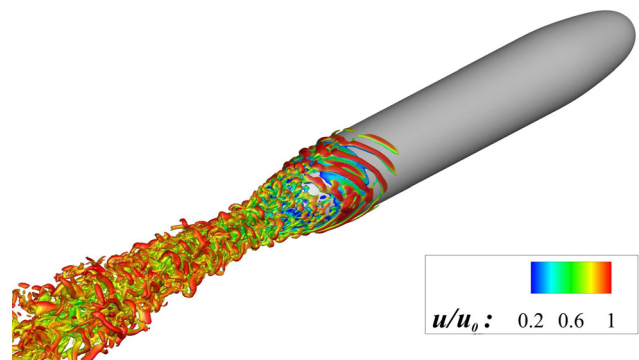


FIG. 4. The wake-flow structures are visualized using the isosurface of the instantaneous Q-criterion ( $Q_{iso} = 0.25$ ), and the isosurface is colored by axial velocity. Q invariant is nondimensionalized by  $Q_{ref} = (u_0/D_{ref})^2$ .

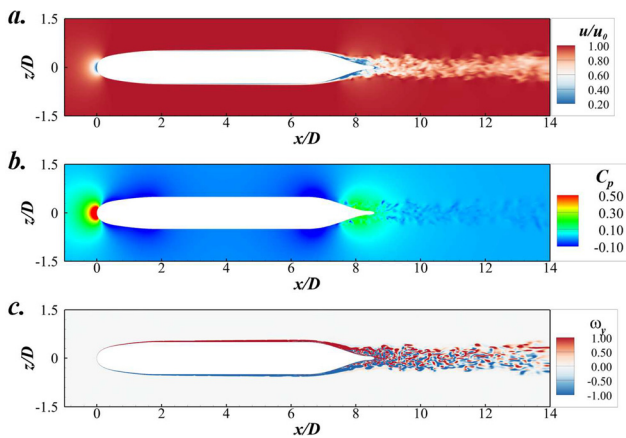


FIG. 5. Instantaneous flow field in the XZ cutoff plane. (a) Axial velocity; (b) pressure coefficient; (c) vorticity magnitude.

velocity profiles as we move downstream. The overall agreement of the predicted results with the available experimental data and the LES results is satisfactory. A small underprediction can be detected in the axial velocity of the IDDES results at  $x/L = 0.904$ , which may be due to the larger flow separation obtained by IDDES. Compared with SST-based IDDES, RSM-based IDDES shows better agreement with both the experimental data and LES results.

Figure 8 compares the profiles of the axial rms-velocity (a) and radial rms-velocity (b) at  $x/L = 0.904, 0.927, 0.956$ , and  $0.978$ . Diamonds denote the measurements taken during the experiment by Huang *et al.*<sup>14</sup> at  $Re_L = 1.2 \times 10^7$ , and only two of four cross-sectional data are available. LES results reported by Kumar and Mahesh<sup>18</sup> and  $k-\omega$ -based DES results reported by Fureby *et al.*<sup>70,71</sup> and Alin *et al.*<sup>51</sup> are also shown for comparison. Notably, both the  $k-\omega$ -based DES and SST-based DES used in the current work overpredict the magnitude of the axial rms-velocity and that of the radial rms-velocity. This trend is also reported by Bhushan *et al.*,<sup>8</sup> who employ the  $k-\omega$ -based IDDES to predict the flow around an appended

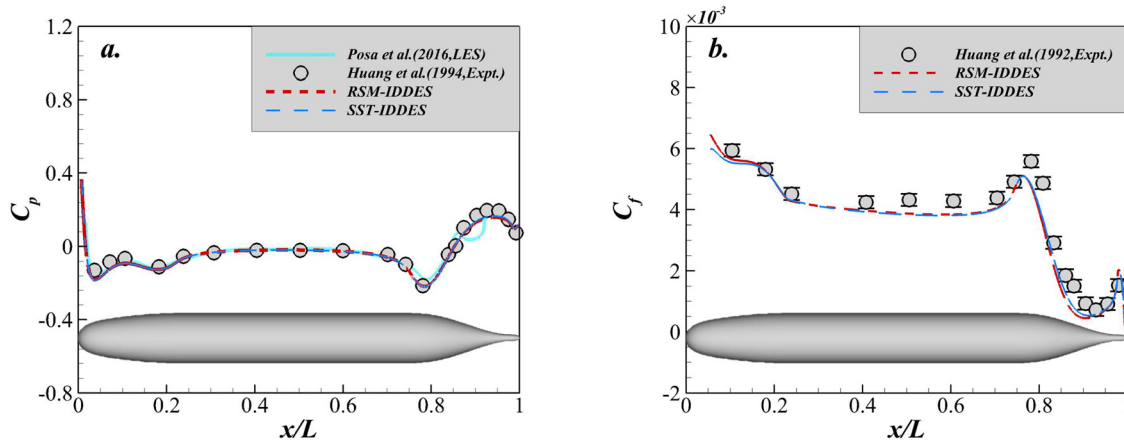


FIG. 6. Distribution of computed mean pressure  $C_p$  (a) and skin-friction  $C_f$  (b) coefficients on the hull. Symbols represent measurements taken from the experiment by Huang *et al.* (1992) at  $Re_L = 1.2 \times 10^7$ , and  $C_f$  measurements are scaled to the Re of current simulations by using a scaling law ( $C_f \sim Re^{-0.2}$ ). The LES results presented by Posa *et al.* (2016) are also shown for comparison.

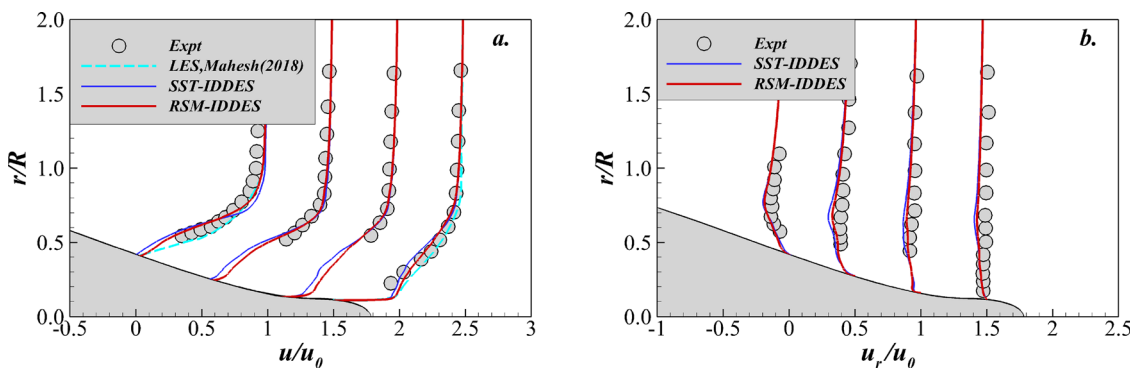
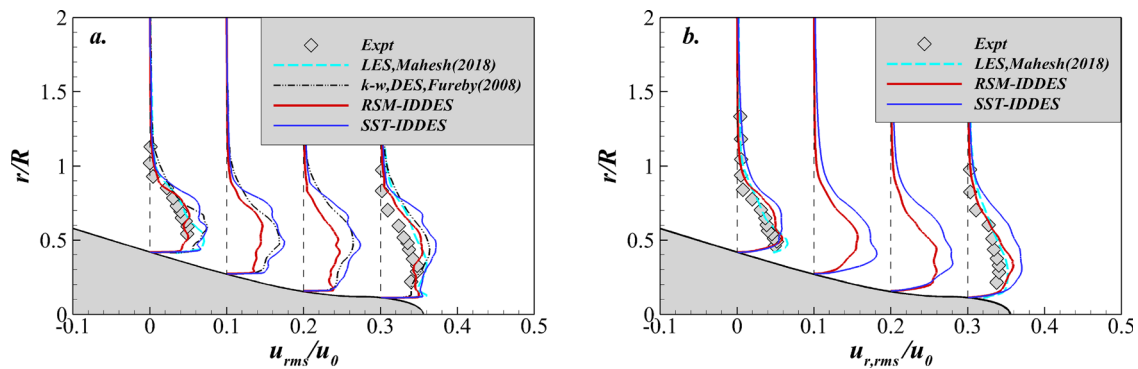


FIG. 7. Time-averaged axial (a) and radial (b) velocity profiles at  $x/L = 0.904, 0.927, 0.956$ , and  $0.978$ . Circles show the measurements taken from the experiment by Huang *et al.* (1992) at  $Re_L = 1.2 \times 10^7$ . The LES results presented by Mahesh *et al.* (2018) are also shown for comparison.



**FIG. 8.** Profiles of the axial rms-velocity (a) and radial rms-velocity (b) at  $x/L = 0.904, 0.927, 0.956,$  and  $0.978$ . Diamonds show the measurements taken from the experiment by Huang *et al.* (1992)  $Re_L = 1.2 \times 10^7$ . The LES results presented by Mahesh *et al.* (2018) are also shown for comparison.

SUBOFF model and obtain a greater magnitude of rms-velocity fluctuations at the stern. The RSM-based IDDES predictions are much better, and reasonably good agreement can be observed with the LES results and experimental data at  $x/L = 0.904$  and  $0.978$ , respectively. This finding is especially true in the predictions of radial rms-velocity, which is considered to be very challenging to capture. Compared with SST-based IDDES or  $k-\omega$ -based DES, RSM-based IDDES predicts the velocity statistics around the stern reasonably better, which can be attributed to the streamwise vortices reproduced by RSM-based IDDES; however, SST-based IDDES fails. As we will discuss below in detail, the circumferential vortices originate from the boundary layer of the stern hull and bring higher momentum fluid toward its wake from the outer layer at azimuthal locations away from the hull. Therefore, RSM-based IDDES predicts a smaller magnitude of fluctuations and shows better agreement with the LES results and experimental data.

**D. Effects of surface curvature**

The boundary layer over the curved surface dominates the flow around SUBOFF. The axisymmetric turbulent boundary layer gradually thickens due to the reverse pressure gradient over the stern, and flows undergo a significant deceleration and eventually separate to form the wake. The unsteadiness of separation is controlled by the turbulent boundary layer<sup>18,20</sup> and the feedback from the separated region to the boundary layer.<sup>20</sup> The interactions between the boundary layer and the separated flows need to be modeled accurately. One of the advantages of the RSM is its greater adherence to fluid dynamical physics than scalar models,<sup>53,54</sup> which could be fully inherited by RSM-based IDDES. The performance of RSM-based IDDES can be evaluated by analysis of the flow near the stern.

Figure 9 presents the fields of turbulent kinetic energy (TKE) in the wake, where the bimodal nature of the turbulence wake can be clearly observed. The TKE was obtained by solving Reynolds-averaged NS equations and could be considered equivalent to the time-averaged flow field. This flow field will be used as the initial solution for the subsequent unsteady IDDES simulations. The dashed lines (a) to (e) show the locations of the data extraction sections at which the turbulent boundary layer quantities will be investigated. The intersection points of the dashed lines (a, b, c, d, e) and the wall are evenly distributed between  $x/L = 0.745$  and  $x/L = 0.978$ , and all these dashed lines are perpendicular to the wall. The turbulent boundary layer on the stern

can be studied from the evolution of TKE. The balanced equation for TKE consists of mean-flow convection, production, dissipation, and viscous diffusion. Among these terms, the dissipation term (its magnitude is proportional to the amplitude of TKE) and the viscous diffusion term have negative or relatively small contributions to the growth of TKE, while only the convection term and production term have positive contributions to the growth of TKE. The comparison of profiles of time-averaged TKE production and convections is plotted in Fig. 10. The magnitude of the production term is greater than that of the convection term for all sections, which reveals that the production term is the dominant source of TKE.

Surface curvature can suppress or amplify turbulence, depending on whether it has a convex or concave curvature. Figure 11 presents the schematic of curved surfaces and the projection of streamlines. The turbulent boundary layer develops on a surface with convex curvature followed by a section of concave curvature. Since the development of the turbulence boundary layer along the stern is mainly dominated by the production of TKE, the performance of the RSM and the eddy-viscosity models for predictions can be understood qualitatively by examining the formulation for the production term in

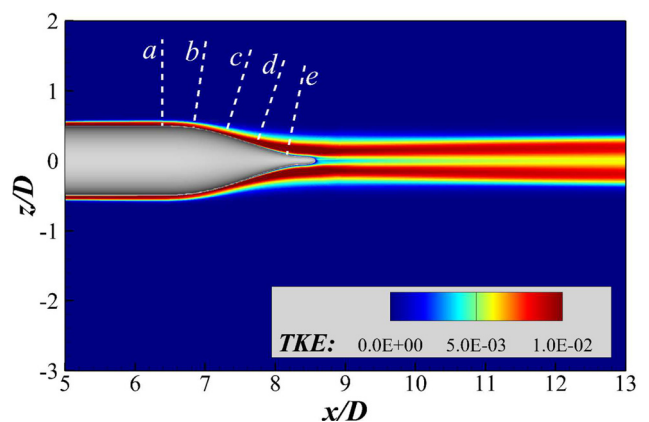


**FIG. 9.** Fields of turbulent kinetic energy (TKE) in the wake. The dashed line shows the locations of the data extraction sections at which the turbulence production and convection were extracted. The intersection points of the dashed lines (a, b, c, d, e) and the wall are evenly distributed between  $x/D = 6.39$  and  $x/D = 8.39$  (after body section), and these dashed lines are perpendicular to the wall.

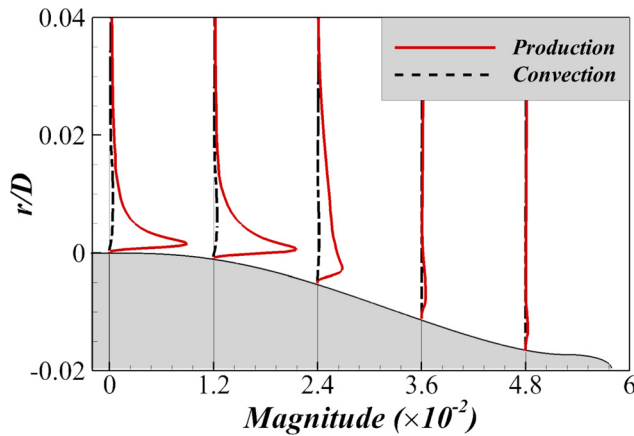


FIG. 10. Profiles of time-averaged TKE production and convections.

these equations. On a curved wall, it is more convenient to express the velocity gradient and stress tensor in polar coordinates  $(r, \theta)$ , as shown in Fig. 11. Let  $\tilde{u}_\theta, \tilde{u}_r$  represent the velocity in the circumferential and radial directions, respectively. The velocity and Reynolds stress tensor in polar coordinates are obtained by a conversion from the data in the rectangular coordinates ( $y = 0$  plane), the velocity gradient in the polar coordinates is calculated by a simple central difference method. For an isotropic eddy-viscosity model, neglecting second-order small terms, the production rate of turbulent kinetic energy is given by

$$P_{k,SST} = \mu_t \left( \frac{\partial \tilde{u}_\theta}{\partial r} - \frac{\tilde{u}_\theta}{r} \right)^2 + 4\mu_t \left( \frac{1}{r} \frac{\partial \tilde{u}_\theta}{\partial \theta} \right)^2. \quad (14)$$

Here,  $\mu_t$  denotes the turbulence eddy viscosity. In the RSM, the production terms are closed. Neglecting the second-order small terms, the production rate of turbulent kinetic energy and shear stress is given by

$$\begin{cases} P_{k,RSM} = \frac{1}{2}(P_{\theta\theta} + P_{rr}) = -2\rho \overline{u'_\theta u'_r} \left( \frac{\partial \tilde{u}_\theta}{\partial r} - \frac{\tilde{u}_\theta}{r} \right) \\ \quad - 2 \left( \overline{\rho u'_\theta u'_\theta} - \overline{\rho u'_r u'_r} \right) \left( \frac{1}{r} \frac{\partial \tilde{u}_\theta}{\partial \theta} \right), \\ P_{\theta r,RSM} = -\overline{\rho u'_r u'_r} \frac{\partial \tilde{u}_\theta}{\partial r} + \overline{\rho u'_\theta u'_\theta} \frac{\tilde{u}_\theta}{r}. \end{cases} \quad (15)$$

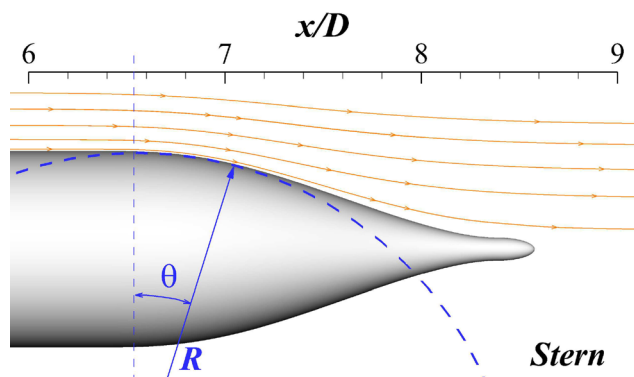
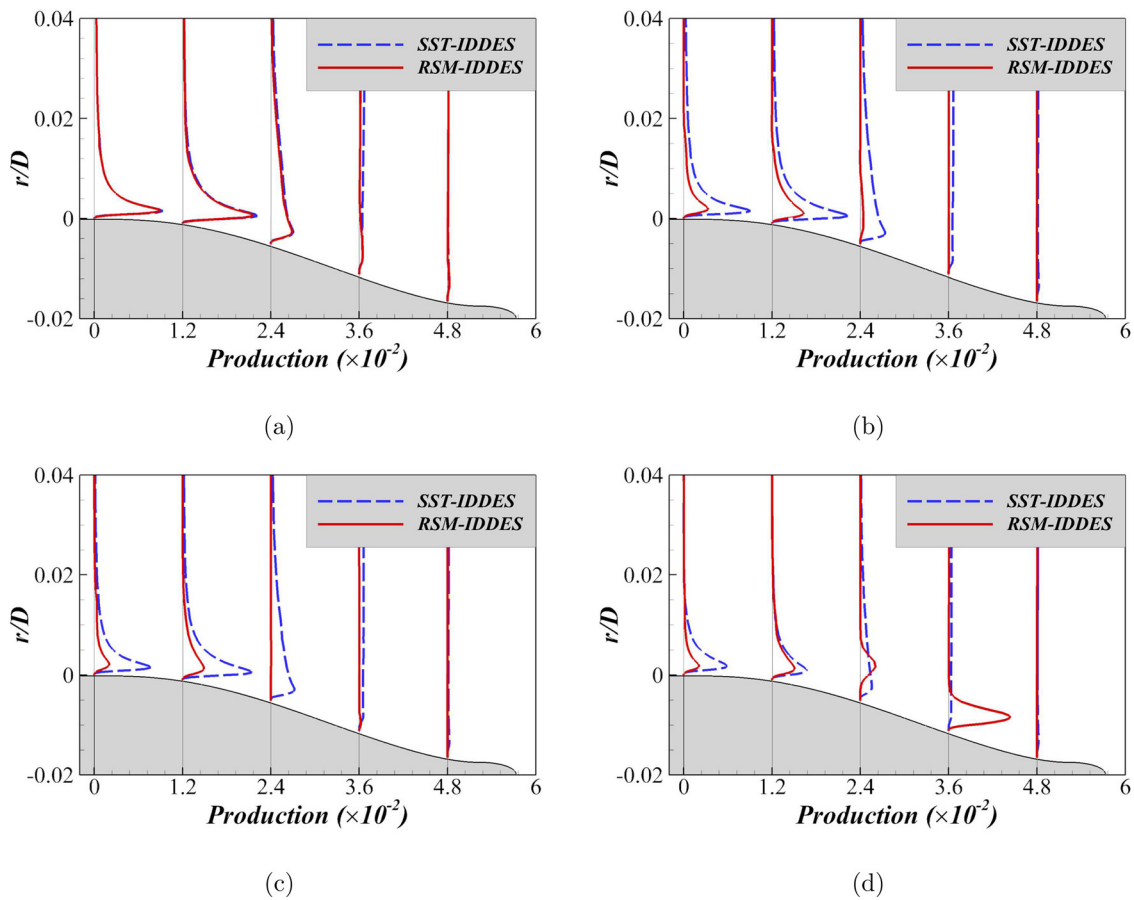


FIG. 11. Side view of the stern showing the schematic of the curved surfaces and the projection of streamlines.

The variations in the TKE production rate are monitored at five extraction sections, whose locations are shown in Fig. 9 and correspond to dashed lines (a) to (c). Figure 12 shows the profiles of TKE production predicted by SST-based IDDES and RSM-based IDDES at four uniform spacing steps, and the corresponding velocity profiles are plotted in Fig. 13. These data are obtained by unsteady simulations with the same initial solution as that shown in Fig. 9 and with the same numerical settings except the turbulence model. TKE production varies spatially and over time, as shown in Fig. 12. At  $t = 0$ , the maximum TKE production in the boundary layer decreases along the streamwise direction [Fig. 12(a)] because the velocity gradient  $(\partial \tilde{u}_\theta / \partial r)$  in the radial direction decreases as the flows move downstream. Evidence can be found in Fig. 13(a) that the turbulent boundary layer gradually grows due to the adverse pressure gradient in this region. Considering Eqs. (14) and (15),  $\partial \tilde{u}_\theta / \partial r \sim O(u/\delta)$ ,  $\tilde{u}_\theta / r \sim O(u/R)$ ,  $\delta$  and  $R$  are the thickness of the boundary layer and the radius of curvature, respectively. Therefore,  $\partial \tilde{u}_\theta / \partial r$  is greater than  $\tilde{u}_\theta / r$ . Figure 14 presents the profiles of Reynolds shear stress in the turbulent boundary layer at  $t = 0$ . The decrease in  $\partial \tilde{u}_\theta / \partial r$  acts to diminish the production of TKE by mean shear.

Similarly, we can deduce that the ratio of  $P_{\theta\theta}/P_{rr}$  is roughly equivalent to  $R/\delta$  in the boundary layer, and the streamwise component Reynolds stress  $\overline{\rho u'_\theta u'_\theta}$  is greater than the normal component  $\overline{\rho u'_r u'_r}$  at the junction of the mid-body and stern. Considering Eq. (15),  $(\overline{\rho u'_\theta u'_\theta} - \overline{\rho u'_r u'_r}) > 0$ , an increase in streamwise velocity means a positive gradient  $\partial \tilde{u}_\theta / \partial \theta$ , which leads to a reduction in the production of TKE. Figure 15 depicts the directional derivative of streamwise velocity along the colored line which is defined by a piecewise function in XZ-plane. One can observe that the streamwise velocity increases at the junction of the mid-body and stern then decreases downstream. A negative gradient of streamwise velocity downstream will result in an enhancement of the production rate. Therefore, the production of TKE decreases with time at line (a) and line (b) but increases with time at line (d) and line (e). A similar trend but smaller amplitude can be observed for SST-based IDDES at the junction of the mid-body and stern because the 1st term of Eq. (14) does decrease in convex curved flows, and then, some effects of curvature should be captured. However, the second terms in Eq. (14) are always positive, which will always increase turbulence even in the case of flow acceleration. Evidence can also be found in Fig. 16, which shows that the instantaneous contours of the TKE overlapped with the projection of streamlines at  $t = 0.84\Delta t^*$ . For clarity, only the lower part ( $z/D < 0$ ) of the projection streamlines is shown here. The SST-based IDDES predicts limited turbulent motions with some fluctuations of annular TKE distributed around the stern, and this initial transient still requires more physical time steps to die out. While RSM-based IDDES is more sensitive to curvature surfaces, the unsteadiness of flow motions induced by boundary layer separation is observed in the prediction [see Fig. 16(a)]. Thus, the RSM-based IDDES can provide a better response of the turbulent boundary layer to such flow over curvature walls in the relatively early stage of the simulation.

Figure 17 presents the instantaneous contours of the TKE overlapping with the projection of streamlines at  $t = 10.02\Delta t^*$ , when the flow was relatively fully developed. The large-scale turbulent motions near the stern are provided by flow visualization, with examples of a mixing layer and axisymmetric wakes. Additionally, the projection of the streamlines is shown in the lower part ( $z/D < 0$ ) to highlight the



**FIG. 12.** Profiles of TKE production predicted by SST-based IDDES and RSM-based IDDES at four uniform spacing steps,  $t=0$  (a),  $t=0.28\Delta t^*$  (b),  $t=0.56\Delta t^*$  (c),  $t=0.84\Delta t^*$  (d).

presence of streamwise vortices. On the  $y=0.0$  plane, SST-based IDDES appears to provide a larger separated region than RSM-based IDDES, and the vortical structure developing from the upstream boundary layer shows a stronger influence on the flows around the stern and downstream wake. While RSM-based IDDES predicts a weaker separation with some streamwise vortices evenly distributed in the circumferential direction, evidence is shown on the  $y=0.0$  plane and  $x/D=7.72$  cross section in Fig. 16. These vortices have similar sizes and bring high-momentum fluid toward the wall, creating a “fuller” mean velocity profile near the concave wall (see Fig. 7). The counterrotating vortices send low-momentum flow away from the boundary layer; hence, flow separation is suppressed to some extent, by which the RSM-based IDDES avoids overpredicting the fluctuation of velocity near the stern and results in better agreements with wall-resolved LES results and the measurements (see Fig. 8). Therefore, we could deduce that exact production terms in RSM-based IDDES are capable of capturing the strong interaction between individual stress and the streamline curvature.

#### IV. SUMMARY AND CONCLUSION

Flows around SUBOFF body without appendages have been studied using a hybrid RANS/LES approach. This approach is based

on the SSG/LRR- $\omega$  RSM and a modification to the length scale. The flows around the SUBOFF body at  $Re_L = 1.2 \times 10^6$  and a zero yaw angle is considered. Three typical grids with different resolutions were generated and tested to determine the mesh convergence. The results, including the time-averaged  $C_p$ ,  $C_f$  velocity profile, and rms-velocity profiles, are in good agreement with experimental data and available LES results, and the overall agreement of the comparisons was satisfactory. To assess the performance of the RSM-based IDDES, we performed an SST-based IDDES simulation under identical free-stream conditions and introduced the predictions reported in the literature using  $k-\omega$ -based DDES for comparisons. The sensitivity of the hybrid approaches to the RANS models was observed for separated flow with surface curvature and adverse pressure gradient-induced separation, which indicates the importance of the RANS model in a DES approach. The RSM-based IDDES model was found to provide good agreement on the velocity fluctuations with the experimental data and LES results.

The features of the flow reported in the experiment and the literature have been reproduced by RSM-based IDDES well. The flow topology is characterized by an unsteady separated flow that formed on the stern due to the 3D boundary layer under the influence of

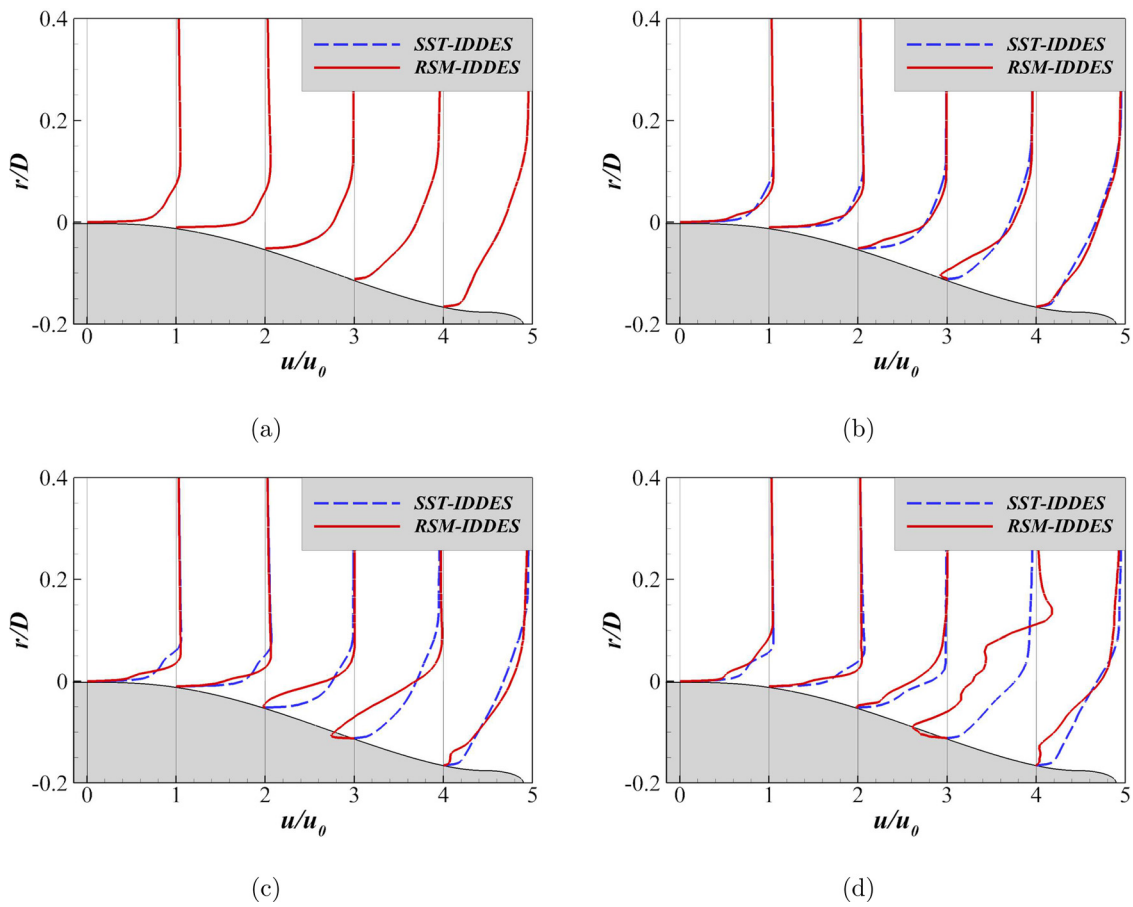


FIG. 13. The magnitude of streamwise velocity predicted by SST-based IDDES and RSM-based IDDES at four uniform spacing steps,  $t = 0$  (a),  $t = 0.28\Delta t^*$  (b),  $t = 0.56\Delta t^*$  (c),  $t = 0.84\Delta t^*$  (d). It is noted that the sketch of SUBOFF was used to show the location where the data are extracted.

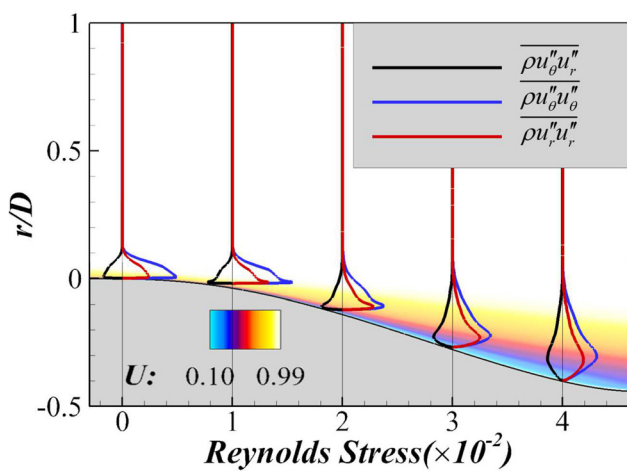


FIG. 14. The profiles of Reynolds stress in the turbulent boundary layer at  $t = 0$ , locations are shown in Fig. 9.

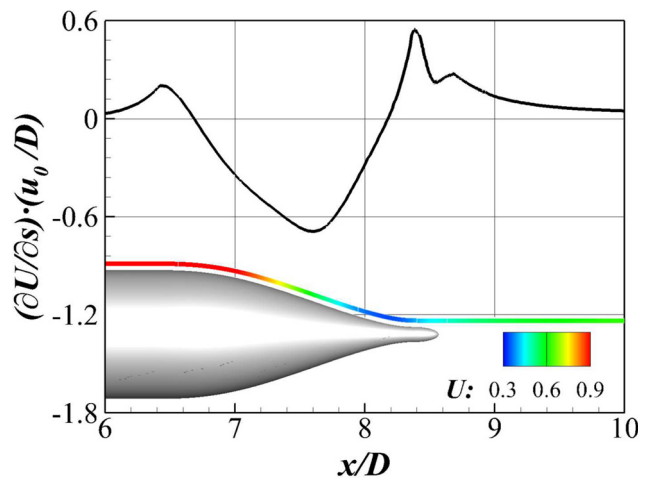
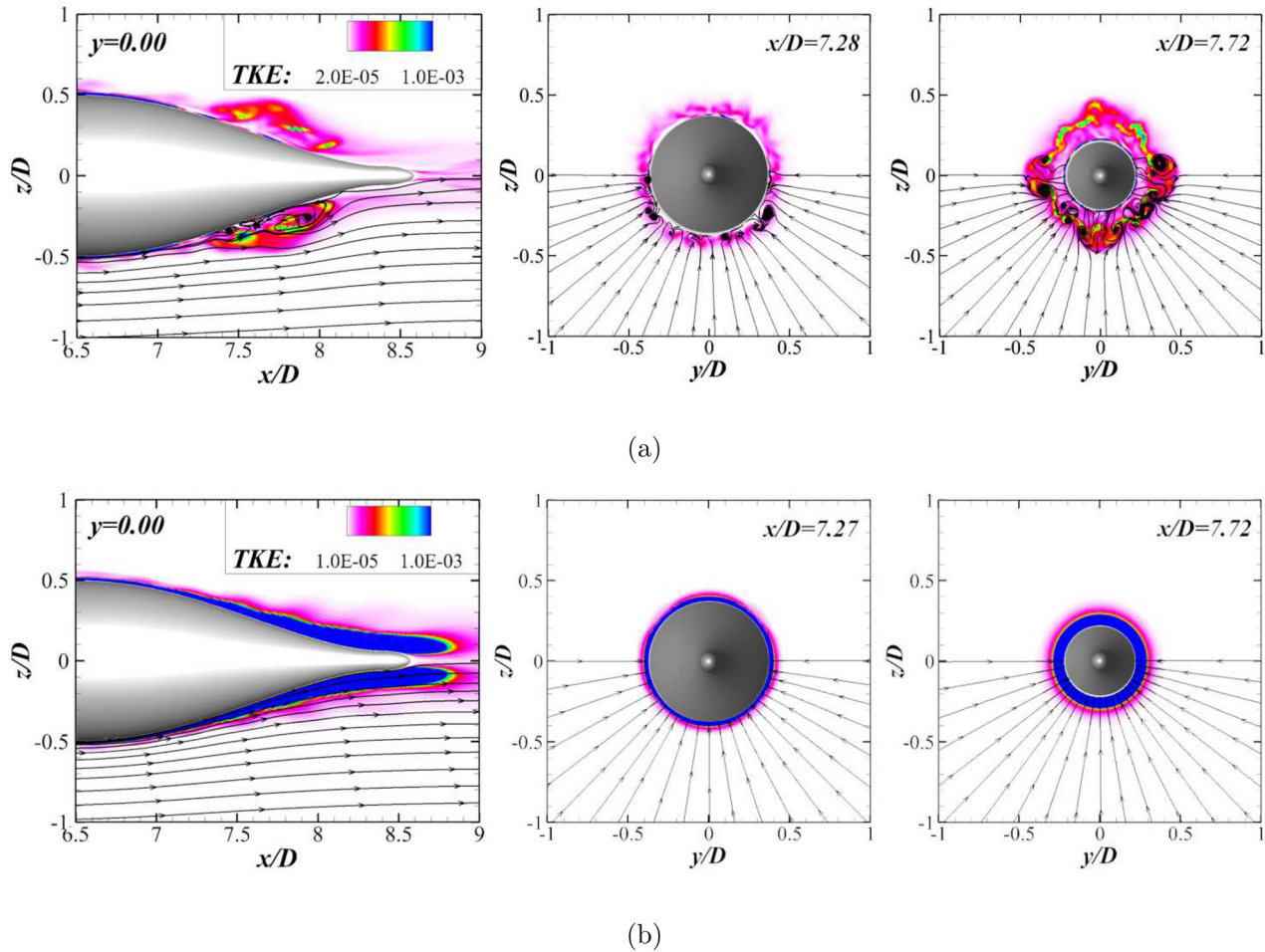


FIG. 15. The directional derivative of streamwise velocity (black line) along the colored line shown below; these data are obtained at  $t = 0$ .



**FIG. 16.** Contours of the TKE overlapping with the projection of streamlines at  $t = 0.84\Delta t^*$ , data obtained by RSM-based IDDES (a), data obtained by SST-based IDDES (b). For clarity, only the lower part ( $z/D < 0$ ) of the streamlines is shown.

pressure gradients and surface curvature. A sequence of vortices interacting with each other in the boundary layer merges together as they are being convected downstream and form the wake. RSM-based IDDES provided a good response of the turbulent boundary layers to the concave and convex curvatures. Near the stern cap, a strong turbulent mixing layer is formed and grows in thickness as the flow develops. This layer mixes the high-momentum fluid in the outer part of the boundary layer with the low-momentum fluid from the near-wall region and tends to suppress the flow separations. The exact production terms in RSM-based IDDES are capable of capturing these processes, which are dynamically important in the near-wall region and show a strong interaction between individual stress and streamline curvature.

**AUTHORS’ CONTRIBUTIONS**

Y.L. and Z.Z. contributed equally to this work.

**ACKNOWLEDGMENTS**

This work was supported by the NSFC Basic Science Center Program for “Multiscale Problems in Nonlinear Mechanics” (Grant

No. 11988102), the National Natural Science Foundation of China (Grant Nos. 11922214 and 91952301), and the National Numerical Windtunnel project. The computations are conducted on Tianhe-1 at the National Supercomputer Center in Tianjin.

**APPENDIX: CALIBRATION OF MODEL COEFFICIENTS**

This calibration process is considered to be an essential prerequisite for DES computation. Decaying isotropic turbulence (DIT) represents the simplest realization of turbulent flow and is therefore a fundamental test case for new turbulence modeling. For this purpose, DIT computations are conducted with various values for  $C_{DES}$ . The employed grid consists of  $64^3$  rectangular and equidistant control volumes. The physical domain is a rectangular box with an edge length of  $2\pi$ , where the lowest and highest resolved wavenumbers are 1 and  $N/2$ , respectively.

Simulations of DIT are performed in a cubic computational domain with periodic boundary conditions in each spatial direction. A second-order full implicit dual time-stepping scheme is adopted,

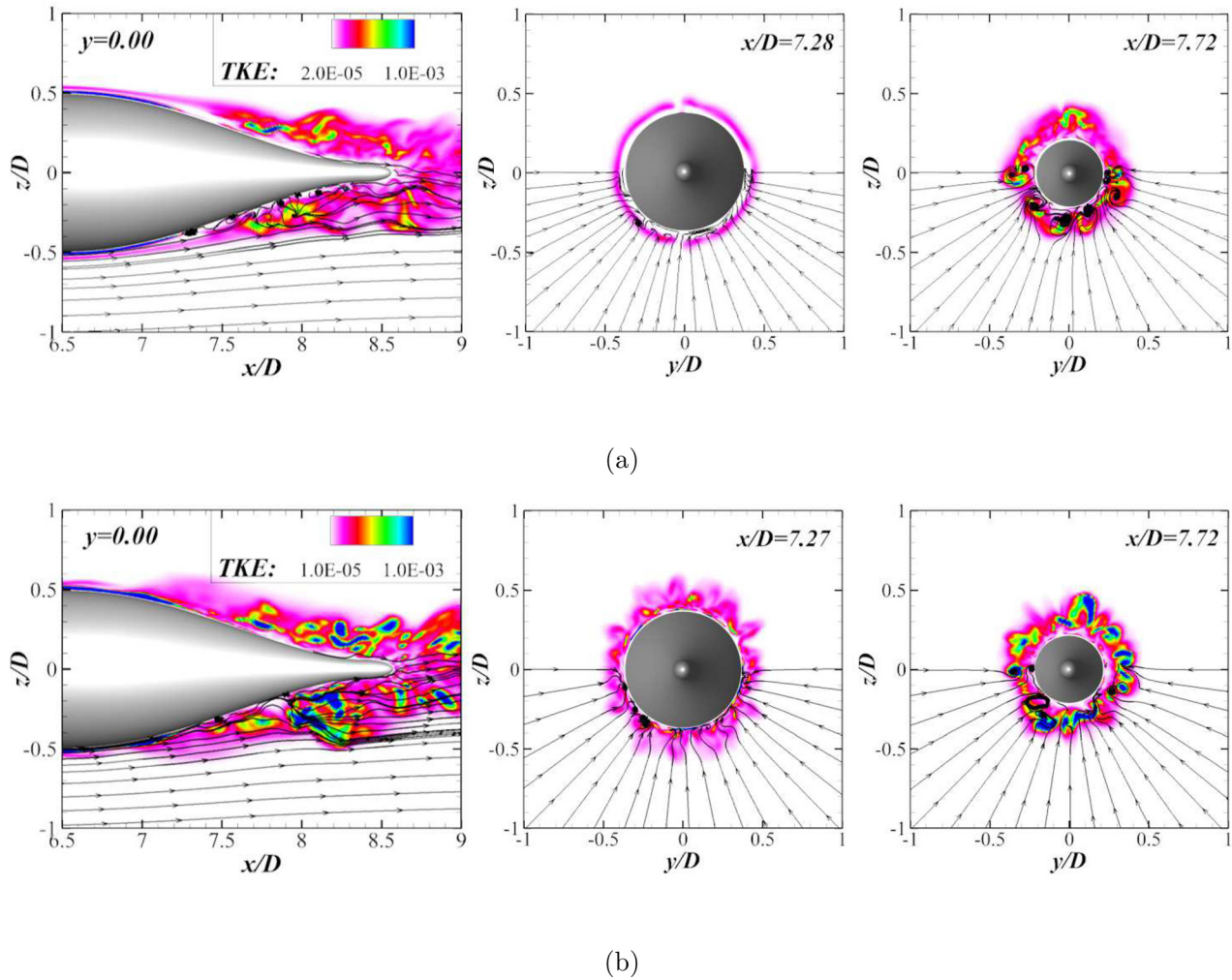


FIG. 17. Contours of the TKE overlapping with the projection of streamlines at  $t = 10.02\Delta t^*$ , data obtained by RSM-based IDDES (a), data obtained by SST-based IDDES (b). For clarity, only the lower part ( $z/D < 0$ ) of the streamlines is shown.

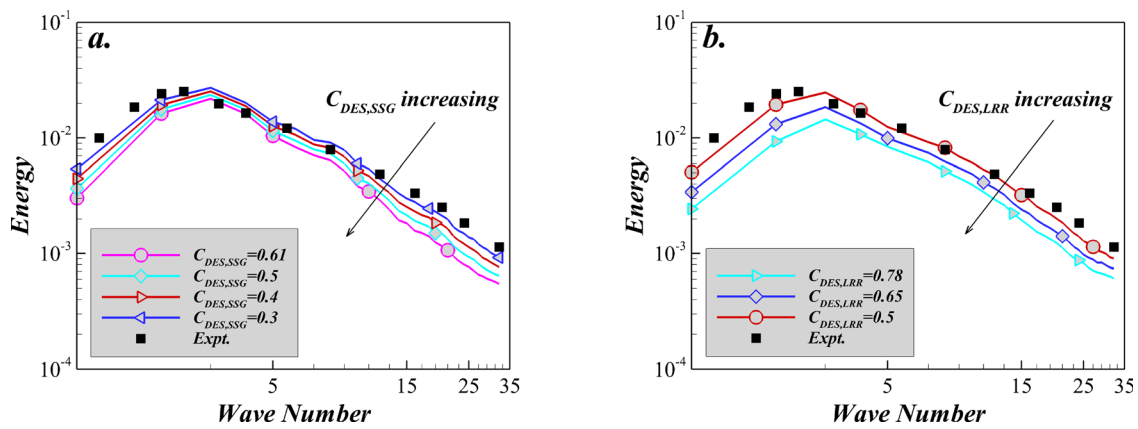


FIG. 18. Effect of different  $C_{DES}$  constants in RSM-based IDDES on the energy spectrum in the DIT case,  $U_0 t/M = 171$ . (a) SSG branch, (b) LRR branch.

with time steps of 0.001 nondimensional units for each case. The velocity field for the solution initialization was obtained from the inverse Fourier transform of the experimental spectra presented by Comte-Bellot and Corrsin.<sup>72</sup> The RANS model in current DES methods contains SSG and LRR branches, the final  $C_{DES}$  is blended by the  $F_1$ -function, and therefore,  $C_{DES}$  can be calibrated separately. Figure 18 shows the resulting normalized energy spectra over the normalized wavenumber for different  $C_{DES}$  values at  $U_0 t/M = 171$ . In the DIT case,  $U_0$  represents the airspeed approaching the measuring section, and  $M$  denotes the size of the measuring section. The results obtained by  $C_{DES,SSG} = 0.3$  and  $C_{DES,LRR} = 0.5$  agree well with the measured spectra. Since only the LES mode of the DES is affected, the calibration is independent of the DES, DDES, and IDDES formulations and therefore applies to both RSM-DES and RSM-DDES. The coefficients in SST-based IDDES model were also calibrated in a similar way, and the values of  $C_{DES,k-\omega} = 0.56$  and  $C_{DES,k-\epsilon} = 0.45$  were found to be satisfactory.

## DATA AVAILABILITY

The data that support the findings of this study are available from the corresponding author upon reasonable request.

## REFERENCES

- C. Fureby, "Challenges for large eddy simulation of engineering flows," in *Whither Turbulence and Big Data in the 21st Century?* (Springer, 2017), pp. 375–400.
- Y.-X. Zhang, X.-P. Wu, Z.-Y. Zhou, X.-K. Cheng, and Y.-L. Li, "A numerical study on the interaction between forward and aft propellers of hybrid CRP pod propulsion systems," *Ocean Eng.* **186**, 106084 (2019).
- J. Jiang, J.-T. Qi, H. Cai, K. Chen, and W.-X. Huang, "Prediction and optimisation of low-frequency discrete-and broadband-spectrum marine propeller forces," *Appl. Ocean Res.* **98**, 102114 (2020).
- Z. Liu, Y. Xiong, and C. Tu, "Method to control unsteady force of submarine propeller based on the control of horseshoe vortex," *J. Ship Res.* **56**, 12–22 (2012).
- H. Yao, H. Zhang, H. Liu, and W. Jiang, "Numerical study of flow-excited noise of a submarine with full appendages considering fluid structure interaction using the boundary element method," *Eng. Anal. Boundary Elem.* **77**, 1–9 (2017).
- Z. Liu, Y. Xiong, and C. Tu, "Numerical simulation and control of horseshoe vortex around an appendage-body junction," *J. Fluids Struct.* **27**, 23–42 (2011).
- N. Chase and P. M. Carrica, "Submarine propeller computations and application to self-propulsion of DARPA SUBOFF," *Ocean Eng.* **60**, 68–80 (2013).
- S. Bhushan, M. Alam, and D. Walters, "Evaluation of hybrid RANS/LES models for prediction of flow around surface combatant and suboff geometries," *Comput. Fluids* **88**, 834–849 (2013).
- D. Feng, X. Wang, F. Jiang, and Z. Zhang, "Large eddy simulation of DARPA SUBOFF for  $Re = 2.65 \times 10^7$ ," *J. Coastal Res.* **73**, 687–691 (2015).
- S. Wang, B. Shi, Y. Li, and G. He, "A large eddy simulation of flows around an underwater vehicle model using an immersed boundary method," *Theor. Appl. Mech. Lett.* **6**, 302–305 (2016).
- L. Cao, J. Zhu, and G. Zeng, "Viscous-flow calculations of submarine maneuvering hydrodynamic coefficients and flow field based on same grid topology," *J. Appl. Fluid Mech.* **9**, 817 (2016).
- J. Zhang, G. Minelli, A. N. Rao, B. Basara, R. Bensow, and S. Krajnović, "Comparison of PANS and LES of the flow past a generic ship," *Ocean Eng.* **165**, 221–236 (2018).
- N. A. Balantrapu, D. J. Fritsch, A. J. Millican, C. Hickling, A. Gargiulo, V. Vishwanathan, W. N. Alexander, and W. J. Devenport, "Wall pressure fluctuations in an axisymmetric turbulent boundary layer under strong adverse pressure gradient," AIAA Paper No. 2020-0572, 2020.
- T. T. Huang, H.-L. Liu, N. C. Grooves, T. J. Forlini, J. N. Blanton, and S. Gowing, "Measurements of flows over an axisymmetric body with various appendages in a wind tunnel: The DARPA SUBOFF experimental program," in *Proceedings of the 19th Symposium on Naval Hydrodynamics* (National Academy Press, Seoul, Korea, 1994), p. 321.
- J. M. Jiménez, M. Hultmark, and A. J. Smits, "The intermediate wake of a body of revolution at high Reynolds numbers," *J. Fluid Mech.* **659**, 516–539 (2010).
- J. M. Jiménez, R. T. Reynolds, and A. J. Smits, "The effects of fins on the intermediate wake of a submarine model," *J. Fluids Eng.* **132**, 031102 (2010).
- A. Posa and E. Balaras, "A numerical investigation of the wake of an axisymmetric body with appendages," *J. Fluid Mech.* **792**, 470–498 (2016).
- P. Kumar and K. Mahesh, "Large-eddy simulation of flow over an axisymmetric body of revolution," *J. Fluid Mech.* **853**, 537–563 (2018).
- A. Posa and E. Balaras, "A numerical investigation about the effects of Reynolds number on the flow around an appended axisymmetric body of revolution," *J. Fluid Mech.* **884**, A41 (2020).
- D. Zhou, K. Wang, and M. Wang, "Large-eddy simulation of an axisymmetric boundary layer on a body of revolution," AIAA Paper No. 2020-2989, 2020.
- M. Liefvendahl and C. Fureby, "Grid requirements for LES of ship hydrodynamics in model and full scale," *Ocean Eng.* **143**, 259–268 (2017).
- L. Wang, R. Hu, and X. Zheng, "A comparative study on the large-scale-resolving capability of wall-modeled large-eddy simulation," *Phys. Fluids* **32**, 035102 (2020).
- F. Stern, J. Yang, Z. Wang, H. Sadat-Hosseini, M. Mousaviraad, S. Bhushan, and T. Xing, "Computational ship hydrodynamics: Nowadays and way forward," *Int. Shipbuilding Prog.* **60**, 3–105 (2013).
- S. Bhushan, P. Carrica, J. Yang, and F. Stern, "Scalability studies and large grid computations for surface combatant using CFDShip-Iowa," *Int. J. High Perform. Comput. Appl.* **25**, 466–487 (2011).
- F. Stern, Z. Wang, J. Yang, H. Sadat-Hosseini, M. Mousaviraad, S. Bhushan, M. Diez, Y. Sung-Hwan, P.-C. Wu, S. M. Yeon *et al.*, "Recent progress in CFD for naval architecture and ocean engineering," *J. Hydrodyn.* **27**, 1–23 (2015).
- L. Liu, M. Chen, J. Yu, Z. Zhang, and X. Wang, "Full-scale simulation of self-propulsion for a free-running submarine," *Phys. Fluids* **33**, 047103 (2021).
- P. R. Spalart, "Detached-eddy simulation," *Annu. Rev. Fluid Mech.* **41**, 181–202 (2009).
- D. Drikakis, D. Kwak, and C. C. Kiris, "Computational aerodynamics: Advances and challenges," *Aeronaut. J.* **120**, 13–36 (2016).
- R. Mokhtarpoor, S. Heinz, and M. Stoellinger, "Dynamic unified RANS-LES simulations of high Reynolds number separated flows," *Phys. Fluids* **28**, 095101 (2016).
- C. Mockett, "A comprehensive study of detached eddy simulation," Ph.D. thesis (Technischen Universität Berlin, 2009).
- P. R. Spalart *et al.*, "Comments on the feasibility of LES for wings, and on a hybrid RANS/LES approach," in *Proceedings of First AFOSR International Conference on DNS/LES* (Greyden Press, 1997), p. 137–148.
- P. R. Spalart, S. Deck, M. L. Shur, K. D. Squires, M. K. Strelets, and A. Travin, "A new version of detached-eddy simulation, resistant to ambiguous grid densities," *Theor. Comput. Fluid Dyn.* **20**, 181–195 (2006).
- M. L. Shur, P. R. Spalart, M. K. Strelets, and A. K. Travin, "A hybrid RANS-LES approach with delayed-DES and wall-modelled LES capabilities," *Int. J. Heat Fluid Flow* **29**, 1638–1649 (2008).
- J. Riou, E. Garnier, S. Deck, and C. Basdevant, "Improvement of delayed-detached eddy simulation applied to separated flow over missile fin," *AIAA J.* **47**, 345–360 (2009).
- M. Strelets, "Detached eddy simulation of massively separated flows," AIAA Paper No. 2001-0879, 2001.
- Z. Yin, K. Reddy, and P. A. Durbin, "On the dynamic computation of the model constant in delayed detached eddy simulation," *Phys. Fluids* **27**, 025105 (2015).
- Z. Yin and P. Durbin, "Adaptive detached eddy simulation of jet in cross flow," AIAA Paper No. 2017-0748, 2017.
- C. He, Y. Liu, and S. Yavuzkurt, "A dynamic delayed detached-eddy simulation model for turbulent flows," *Comput. Fluids* **146**, 174–189 (2017).
- C. He and Y. Liu, "A dynamic detached-eddy simulation model for turbulent heat transfer: Impinging jet," *Int. J. Heat Mass Transfer* **127**, 326–338 (2018).
- D. Mylonas and P. Sayer, "The hydrodynamic flow around a yacht keel based on LES and DES," *Ocean Eng.* **46**, 18–32 (2012).
- S. Sun, C. Wang, C. Guo, Y. Zhang, C. Sun, and P. Liu, "Numerical study of scale effect on the wake dynamics of a propeller," *Ocean Eng.* **196**, 106810 (2020).

- <sup>42</sup>O. Usta and E. Korkut, "Prediction of cavitation development and cavitation erosion on hydrofoils and propellers by detached eddy simulation," *Ocean Eng.* **191**, 106512 (2019).
- <sup>43</sup>L. Wang, R. Hu, L. Li, and S. Fu, "Detached-eddy simulations for active flow control," *AIAA J.* **56**, 1447–1462 (2018).
- <sup>44</sup>J. Liu and Z. Xiao, "Low-frequency oscillation over NACA0015 airfoil near stall at high Reynolds number," *AIAA J.* **58**, 53–60 (2020).
- <sup>45</sup>Y. Liu, G. Wang, H. Zhu, and Z. Ye, "Numerical analysis of transonic buffet flow around a hammerhead payload fairing," *Aerosp. Sci. Technol.* **84**, 604–619 (2019).
- <sup>46</sup>H.-D. Yao and L. Davidson, "Vibro-acoustics response of a simplified glass window excited by the turbulent wake of a quarter-spherocylinder body," *J. Acoust. Soc. Am.* **145**, 3163–3176 (2019).
- <sup>47</sup>M. Xiao and Y. Zhang, "Assessment of the SST-IDDES with a shear-layer-adapted subgrid length scale for attached and separated flows," *Int. J. Heat Fluid Flow* **85**, 108653 (2020).
- <sup>48</sup>Y. Ohmichi, K. Kobayashi, and M. Kanazaki, "Numerical investigation of wake structures of an atmospheric entry capsule by modal analysis," *Phys. Fluids* **31**, 074105 (2019).
- <sup>49</sup>C. He, L. Gan, and Y. Liu, "Dynamics of compact vortex rings generated by axial swirlers at early stage," *Phys. Fluids* **32**, 045104 (2020).
- <sup>50</sup>Y. Fan, C. Xia, S. Chu, Z. Yang, and O. Cadot, "Experimental and numerical analysis of the bi-stable turbulent wake of a rectangular flat-backed bluff body," *Phys. Fluids* **32**, 105111 (2020).
- <sup>51</sup>N. Alin, R. Bensow, C. Fureby, T. Huuva, and U. Svanberg, "Current capabilities of DES and LES for submarines at straight course," *J. Ship Res.* **54**, 184–196 (2010).
- <sup>52</sup>R. Manceau and K. Hanjalić, "Elliptic blending model: A new near-wall Reynolds-stress turbulence closure," *Phys. Fluids* **14**, 744–754 (2002).
- <sup>53</sup>B. E. Launder, "Second-moment closure: Present and future?," *Int. J. Heat Fluid Flow* **10**, 282–300 (1989).
- <sup>54</sup>S. B. Pope, *Turbulent Flows* (Cambridge University Press, Cambridge, UK, 2001), Chap. 11.
- <sup>55</sup>J. Blazek, *Computational Fluid Dynamics: Principles and Applications*, 3rd ed. (Joe Hayton, Sankt Augustin, Germany, 2015), Chap. 2.
- <sup>56</sup>R.-D. Cécora, R. Radespiel, B. Eisfeld, and A. Probst, "Differential Reynolds-stress modeling for aeronautics," *AIAA J.* **53**, 739–755 (2015).
- <sup>57</sup>G. Wang and Z. Ye, "Mixed element type unstructured grid generation and its application to viscous flow simulation," in Proceedings of 24th International Congress of Aeronautical Sciences, Yokohama, Japan, 2004.
- <sup>58</sup>Y. Liu, G. Wang, and Z. Ye, "Dynamic mode extrapolation to improve the efficiency of dual time stepping method," *J. Comput. Phys.* **352**, 190–212 (2018).
- <sup>59</sup>Y. Liu, "Turbulence modeling and its uncertainty quantification for complex aerodynamic flows," Ph.D. thesis (Northwestern Polytechnical University, 2020).
- <sup>60</sup>N. T. Frink, "Upwind scheme for solving the Euler equations on unstructured tetrahedral meshes," *AIAA J.* **30**, 70–77 (1992).
- <sup>61</sup>Z. Xiao, J. Liu, J. Huang, and S. Fu, "Numerical dissipation effects on massive separation around tandem cylinders," *AIAA J.* **50**, 1119–1136 (2012).
- <sup>62</sup>F. Ducros, V. Ferrand, F. Nicoud, C. Weber, D. Darracq, C. Gacherieu, and T. Poinsot, "Large-eddy simulation of the shock/turbulence interaction," *J. Comput. Phys.* **152**, 517–549 (1999).
- <sup>63</sup>C. G. Speziale, S. Sarkar, and T. B. Gatski, "Modelling the pressure-strain correlation of turbulence: An invariant dynamical systems approach," *J. Fluid Mech.* **227**, 245–272 (1991).
- <sup>64</sup>B. J. Daly and F. H. Harlow, "Transport equations in turbulence," *Phys. Fluids* **13**, 2634–2649 (1970).
- <sup>65</sup>M. S. Gritskevich, A. V. Garbaruk, J. Schütze, and F. R. Menter, "Development of DDES and IDDES formulations for the  $k-\omega$  shear stress transport model," *Flow, Turbul. Combust.* **88**, 431–449 (2012).
- <sup>66</sup>N. C. Groves, T. T. Huang, and M. S. Chang, "Geometric characteristics of DARPA (defense advanced research projects agency) SUBOFF models (DTRC model numbers 5470 and 5471)," Technical Report No. DTRC/SHD-1298-01, David Taylor Research Center Bethesda MD Ship Hydromechanics Department, 1989.
- <sup>67</sup>B. Shi, X. Yang, G. Jin, G. He, and S. Wang, "Wall-modeling for large-eddy simulation of flows around an axisymmetric body using the diffuse-interface immersed boundary method," *Appl. Math. Mech.* **40**, 305–320 (2019).
- <sup>68</sup>R. M. Cummings, S. A. Morton, and D. R. McDaniel, "Experiences in accurately predicting time-dependent flows," *Prog. Aerosp. Sci.* **44**, 241–257 (2008).
- <sup>69</sup>Y. Dubief and F. Delcayre, "On coherent-vortex identification in turbulence," *J. Turbul.* **1**, 011 (2000).
- <sup>70</sup>C. Fureby, "Towards the use of large eddy simulation in engineering," *Prog. Aerosp. Sci.* **44**, 381–396 (2008).
- <sup>71</sup>R. E. Bensow, C. Fureby, M. Liefvendahl, and T. Persson, "A comparative study of RANS, DES and LES," in Proceedings of Twenty-Sixth Symposium on Naval Hydrodynamics, 2006.
- <sup>72</sup>G. Comte-Bellot and S. Corrsin, "Simple Eulerian time correlation of full- and narrow-band velocity signals in grid-generated, 'isotropic' turbulence," *J. Fluid Mech.* **48**, 273–337 (1971).